3D-Nanoprinted Antiresonant Hollow-Core Microgap Waveguide: An on-Chip Platform for Integrated Photonic Devices and Sensors

Johannes Bürger,* Vera Schalles, Jisoo Kim, Bumjoon Jang, Matthias Zeisberger, Julian Gargiulo, Leonardo de S. Menezes, Markus A. Schmidt, and Stefan A. Maier

ACCESS | 📊 Metrics & More | 📖 Article Recommendations | 🔵 Supporting Information

ABSTRACT: Due to their unique capabilities, hollow-core waveguides are playing an increasingly important role, especially in meeting the growing demand for integrated and low-cost photonic devices and sensors. Here, we present the antiresonant hollow-core microgap waveguide as a platform for the on-chip investigation of light-gas interaction over centimeter-long distances. The design consists of hollow-core segments separated by gaps that allow external access to the core region, while samples with lengths up to 5 cm were realized on silicon chips through 3D-nanoprinting using two-photon absorption based direct laser writing. The agreement of mathematical models, numerical simulations and experiments illustrates the importance of the antiresonance effect in that context. Our study shows the modal loss, the effect of gap size and the spectral tuning potential, with highlights including extremely broadband transmission windows (>200 nm), very high contrast resonance (>60 dB), exceptionally high structural openness factor (18%) and spectral control by nanoprinting (control over dimensions with step sizes (i.e., increments) of 60 nm). The application potential was demonstrated in the context of laser scanning absorption spectroscopy of ammonia, showing diffusion speeds comparable to bulk diffusion and a low detection limit. Due to these unique properties, application of this platform can be anticipated in a variety of spectroscopy-related fields, including bioanalytics, environmental sciences, and life sciences.

KEYWORDS: hollow-core waveguide, two-photon direct laser writing, integrated photonics spectroscopy, leaky modes, antiresonance guidance, optical gas sensing
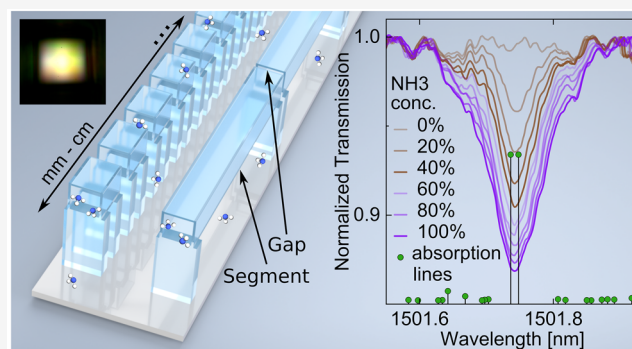
INTRODUCTION

Chip-integration of optical waveguides plays a central role in serving the growing demand for compact, cost-efficient, and mass producible optical devices such as infrared and Raman spectrometers, integrated quantum optical circuits, optofluidic setups, or point-of-care diagnostics. Particularly, gas-based measurements like atmospheric monitoring,[1] breath analysis,[2] or quantum optics with atomic vapors[3] are currently of interest. While the integration of light sources[4−6] and spectrometers[7−9] has seen considerable progress in recent years, less attention has been directed on the waveguide elements in between them. Since the waveguide defines the interaction region between light and analyte, it has a major influence on the properties of the resulting device, like response times, detection limits, or decoherence times of quantum states.

Existing approaches typically suffer from a trade-off between efficient confinement of light to a narrow cross-section and unrestricted access of the analyte to this region. At one end of the spectrum, there are solid core waveguides with completely or partially exposed cores, allowing them to respond immediately to changes in the surrounding medium due to their evanescent fields.[10−12] However, light is guided mostly inside the core, and only a small fraction of the field, the evanescent waves, can be exploited for analyte interactions.[13−15]

The other extreme is represented by hollow-core antiresonant reflecting optical waveguides (ARROWs), where both light and analyte are confined to a hollow core by a sophisticated multilayer cladding.[16−18] This antiresonant approach, which is strongly used in the context of microstructured optical fibers,[19,20] results in nearly complete overlap between the central guided mode and the medium. However, it comes at the cost of poor accessibility of the core volume due to the capillary-type geometry, as complex cladding structures
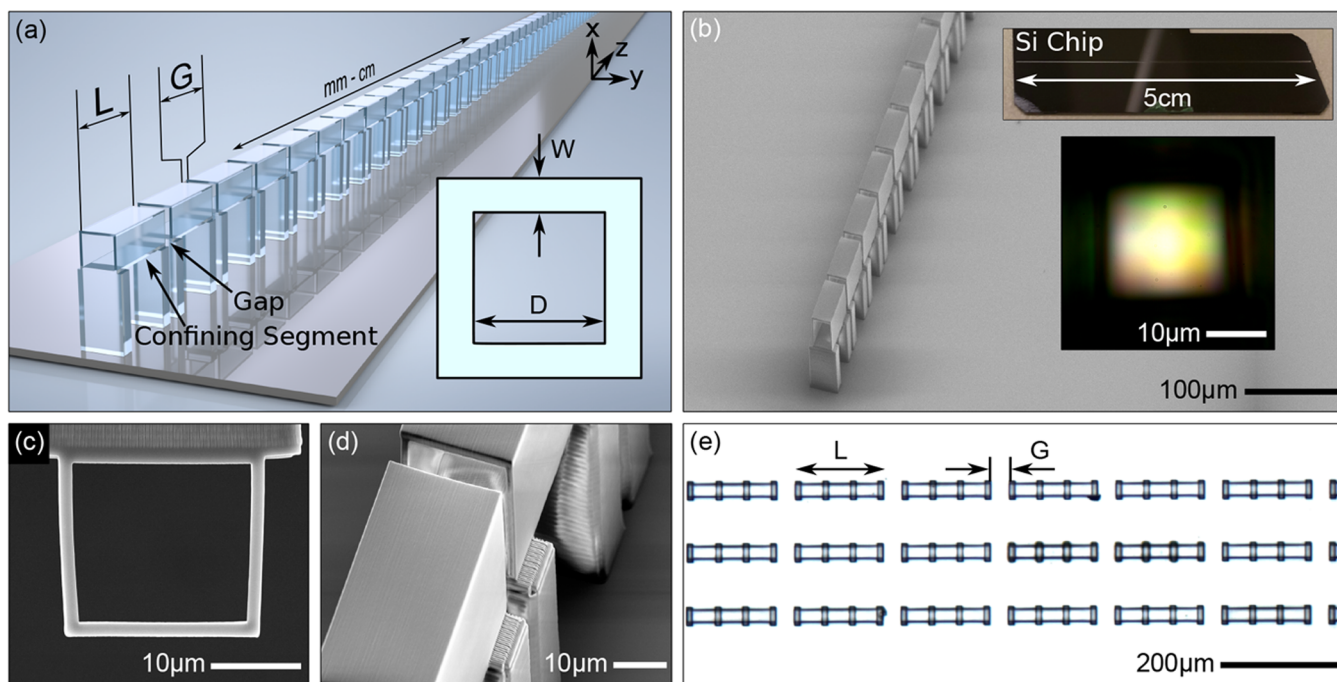
Figure 1. On-chip hollow-core microgap waveguide. (a) Illustration of the waveguides fabricated via 3D-nanoprinting (two-photon absorption based direct laser writing), including the main parameters (gap size G, segment length L, wall thickness W, and core size D. Inset: Square-shaped cross-section. (b−d) Scanning electron microscope (SEM) images of a fabricated structure showing an overview (b), the cross-section (c), and the gap between adjacent elements (d). Note that the dimensions in (b) and (d) are affected by the tilt of the chip during SEM imaging. Insets in (b): Photographic image of a 5 cm long microgap waveguide nanoprinted onto a silicon chip; CCD image of the core mode. (e) Transmission microscopy image of three waveguides (top view).

need to be employed for light confinement.[21] In practice, the passive introduction of analytes into the micron-sized core via diffusion from its end faces is impractically slow, requiring devices to actively pump the analyte through the waveguide, which cannot be integrated straightforwardly.[22] Such filling times are particularly long for low-pressure atomic vapors used in quantum optical experiments and can be on the order of months for a waveguide length of a few centimeters.[3,23,24]

In that context, intermediate solutions in between these two extreme cases have been reported: For instance, single-[25,26] and multislotted waveguides[27] have been developed, where two or more subwavelength-sized solid cores in close proximity provide a larger evanescent field region, thereby increasing the volume of light matter interaction. However, a non-negligible fraction of the field remains inside the waveguide's material, which is an inherent problem to solid core guidance. Since the extent of the evanescent field of such waveguides is wavelength-dependent, complex modal calculations that precisely consider the waveguide geometry are required to modify Lambert−Beer's law for quantitative sensing applications.[28]

On the other hand, techniques have been developed to increase the sidewise accessibility, that is, "openness" of hollow-core waveguides, by introducing lateral holes into their cladding, including femtosecond laser drilling,[29−31] application of heat and pressure,[32] and etching.[33,34] Although such perforated hollow-core waveguides feature orders of magnitude lower analyte exchange times, the inserted holes increase the propagation loss, require an additional lengthy postprocessing step, and can lead to variations between different waveguide batches.

Recently, we showed that additive waveguide fabrication via 3D-nanoprinting using two-photon absorption based direct laser writing (in the text abbreviated as 3D-nanoprinting) of polymeric photoresists can circumvent these issues, realizing hollow-core light cage waveguides with large structural openness while maintaining low propagation loss.[35] Building on this work, we present a novel type of on-chip waveguide that can achieve both a strong light−analyte interaction and fast response times, without requiring advanced multistep fabrication techniques. Our design features two elements that alternate on the micrometer scale, as shown in Figure 1: (1) a square-shaped hollow waveguide segment responsible for confining light via the antiresonance effect and (2) an open gap region allowing fast and straightforward access to the core. The microgap waveguides were successfully implemented up to several cm lengths by 3D-nanoprinting, principally allowing flexible interfacing to other photonic components and low-cost fabrication. All relevant details from the optics perspective, such as propagation loss, tunability of the resonances, and influence of the gaps on transmission, are experimentally revealed and simulated. Furthermore, we developed two analytical models for light guidance in square-core antiresonant waveguides that correctly describe the experimental behavior. To demonstrate the sensing capabilities, tunable diode laser absorption spectroscopy of ammonia gas was performed.

■ RESULTS

Light Guidance in Hollow Square-Shaped Core Waveguides. The light confining segment of our microgap waveguides consists of a hollow square-shaped core with edge length D, surrounded by a polymer wall of thickness W and refractive index n_W (inset of Figure 1a). In the following, we

describe the optical properties of this segment using finite-element simulations and develop two analytical models under the simplification that the waveguide is uniform along its axial dimension, that is, neglecting the gaps.

The simulations reveal broad spectral bands of high transmission, which are delimited by sharp resonances with orders of magnitude higher loss (Figure 2b). For practical applications, the waveguide will be operated in the off-resonance domains, in which losses of about 0.01 dB/mm for visible light are theoretically achievable ($D = 20$ μm, $W = 1$ μm). Simulations of the shape of the fundamental mode show that in these low-loss regions the mode has a square-shaped symmetry and most of the optical power is located inside the core (Figure 2d, image B). Only a small fraction of the power of well below 10^{-3} remains inside the polymer wall (Figure 2c), similar to the previously investigated light cage geometry.[36] Closer to the resonance, the mode spreads out along the polarization direction, transforming to an elliptical shape (Figure 2d, image A). This asymmetric shape arises due to the polarization dependence of the reflections on the confining walls.

The first analytical model, the leaky slab waveguide model, shows that the mechanism of light guidance in microgap waveguides is based on the antiresonance effect:[37,38] Typically cladding modes and core mode phase-match at certain wavelengths (vertical dashed black lines in Figure 2a), leading to large propagation losses due to the removal of power from the core mode. Away from the resonances the wave vector mismatch grows, and low-loss transmission bands occur. Although the losses can be made arbitrarily small, for example, by choosing larger core dimensions,[37] antiresonantly confined modes always dissipate energy during propagation and are therefore referred to as tunneling leaky modes or leaky modes.[39] Such leaky modes are common to many waveguides where light is not guided via total internal reflection, such as ARROWs,[16] hollow-core photonic-crystal fibers,[40,41] or revolver hollow-core fibers.[42]

The leaky slab waveguide model describes the cladding as an infinitely extended flat polymer slab acting as a Fabry−Pérot cavity onto which rays of light from the core mode impinge under a fixed angle (details can be found in the Supporting Information in Section 3.1). For a square-shaped cross-section, both TE- and TM-polarized reflections need to be taken into account in order to correctly resemble the fundamental core mode.[37] Thereby the model takes into account the finite reflectivity of the polymer slab, yielding closed-form expressions for the dispersion (i.e., phase index n_p) and the propagation loss of the fundamental core mode (expressions can be found in the Supporting Information in Section 3.1). In particular, the model shows that the spectral positions of the resonances solely depend on the thickness of the wall W for a given refractive index n_W of the polymer:

$$\lambda_{Res} = \frac{2W}{m}\sqrt{n_W^2 - 1} \ \forall \ m \in \mathbb{N} \tag{1}$$

where m is the order of the resonance, which is equal to the number of field oscillations in the polymer layer. The Fabry−Pérot model accurately predicts the spectral properties of the core mode compared with a full numerical simulation, with small deviations occurring toward longer wavelengths (Figure 2a,b).

As a separate step, we investigated a model that describes the square core as an independent superposition of two
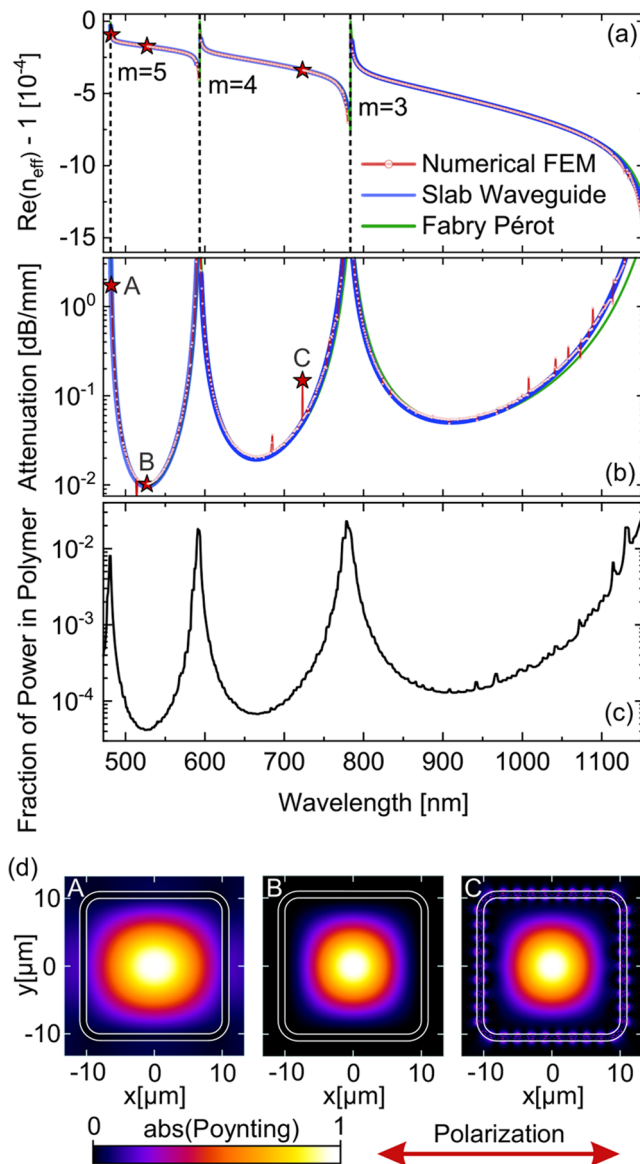

Figure 2. Optical properties of microgap waveguides (theory). (a, b) Spectral distribution of the real part of the effective index (i.e., phase index n_p) and the attenuation of the fundamental core mode (red: 2D Finite-Element simulation of a rounded cross-section of the waveguide; green: Fabry−Pérot model; blue: leaky slab waveguide model). The vertical black dashed lines in (a) denote the position of the cladding resonances (eq 1). All calculations include the material dispersion of the polymer. (c) Median-filtered spectral distribution of the optical power located in the polymer walls normalized to the total power of the mode integrated over the complete simulation region (square with length of 34 μm). (d) Simulated Poynting vector distribution of the core mode at the wavelengths indicated in a/b by the red stars (A: Close to resonance; B: Off-resonance; C: Azimuthal subresonance). Red arrow denotes the polarization of the propagating mode. The calculations were performed for $D = 20$ μm and $W = 1$ μm.

infinitely extended slab waveguides[43] (details can be found in the Supporting Information in Section 3.2) facing each other. Here, the effective indices of the fundamental TE and TM modes of a single slab waveguide were calculated numerically by solving Maxwell's equations with suitable boundary conditions. These were then combined to obtain the complex effective index n_{eff} of the square waveguide while neglecting the
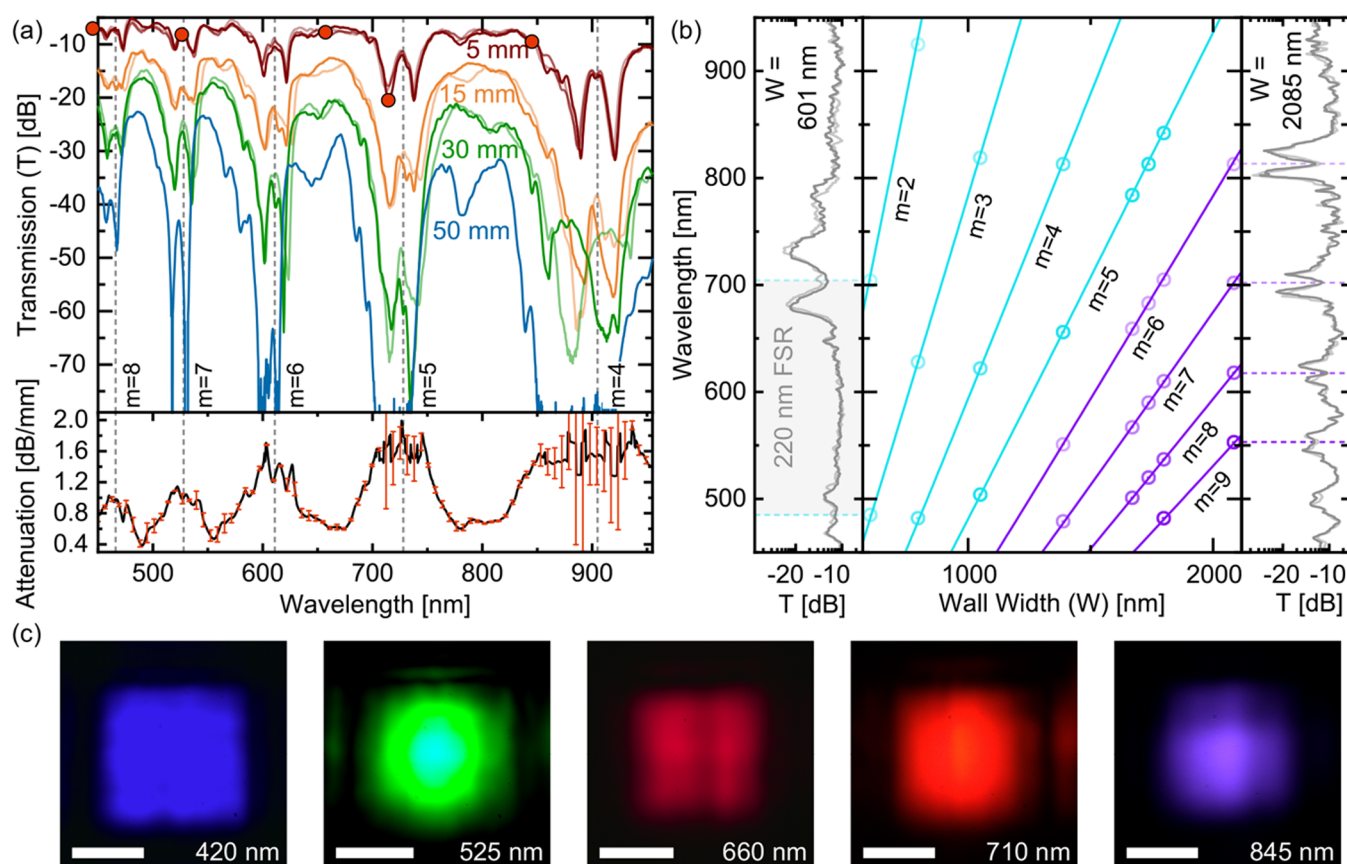
Figure 3. Optical properties of microgap waveguides (experiment). (a) Transmission spectra of waveguide samples ($G = 2\ \mu m$, $L = 176\ \mu m$, $D = 20\ \mu m$, $W = 1.55\ \mu m$) with different total lengths (red, 0.5 cm; orange, 1.5 cm; green, 3 cm; blue, 5 cm). Vertical dashed lines: Theoretical resonance wavelengths of order m obtained from the Fabry−Pérot model. Bottom plot: Spectral distribution of the modal attenuation. Values of copies of a certain structure are shown as curves with lower degree of color saturation. (b) Measured dependence of resonance wavelengths (circles) on wall thickness. Lines show the relation expected from the Fabry−Pérot model. Gray curves show transmission spectra for the lowest ($W = 601\ nm$) and largest ($W = 2085\ nm$) investigated wall widths. (c) Measured mode profiles at selected wavelengths indicated by red circles in (a). Modes between 420 and 710 nm are represented by their true colors, as measured by the camera. Scale bars have a length of $10\ \mu m$.

fields in the corners (Figure S5). Note that this approximation is particularly valid in situations where the core extent is substantially larger than the wavelength λ as for the microgap waveguide investigated here. Furthermore, preliminary simulations show that the exact shape of the corners is irrelevant, both for the position of the resonances and the off-resonance loss (Figure S1). The results of this model (blue lines in Figure 2a,b) yield virtually complete overlap with the full electromagnetic simulation (red lines).

None of the models account for azimuthal resonances (Figure 2d, image C), visible through field oscillations along the long axis of the rectangular cladding elements, which has a length of $D + 2W$. The spectral positions of these azimuthal resonances highly depend on the shape of the corners, where the approximation of having two independent slab waveguides breaks down (Figure S1). As shown in ref 44, these azimuthal resonances do not notably impact the modal characteristics and thus can be neglected for the microgap waveguide.

Design and Implementation of Microgap Waveguides via 3D-Nanoprinting. The microgap waveguides were fabricated directly on silicon chips in a single pass of 3D-nanoprinting using liquid IP-Dip photoresist (see Materials and Methods). As shown in Figure 1a, their design is based on a segmentation approach, where square-shaped hollow waveguide sections alternate with gap regions on the micrometer scale. The entire waveguide is supported from below by a chain of supporting blocks, which makes light guidance independent of potentially rough or tilted substrate surfaces. This design allows quick and reproducible fabrication, with a typical manufacturing time of 10 min per millimeter waveguide length. SEM and transmission microscopy images of the resulting waveguides are shown in Figure 1b−e. We verified the degree of reproducibility of the printing method for a different waveguide geometry, the light cage, showing low chip-to-chip variations of the printed dimensions of about 15 nm.[45] This was done by determining the strand diameter of light cages located on different chips from optical transmission measurements using a well-established formula that relates the resonance wavelengths to the strand diameter (related to the cutoff wavelengths of LP modes of isolated polymer strands).[35] An overview of fabrication inaccuracies and their impact on the waveguide properties can be found in Table 1. Combined with the accessibility of all three spatial dimensions offered by 3D-nanoprinting, the parameters of microgap waveguides can be straightforwardly adapted to the requirements of a certain application. This flexibility is used here to investigate the impact of changing wall thickness W (600 nm to 2 μm), core size D (10−20 μm), gap length G (2−40 μm), and segment length L (45 μm to 1 mm). The maximum waveguide length reached is 5 cm (see inset image in Figure 1b). If not stated

otherwise, a sample length of 5 mm was used for the optical experiments.

In order to quantify the amount of open space for side-wise accessing the core, we calculated the structural openness factor (SOF) for all fabricated devices. The SOF is defined here as the fraction of the surface area of the waveguide that is open to the environment[35] which in this case is given by SOF = $G/(L + G)$. Fully functional samples with SOFs ranging from 0.2% to 18% were fabricated.

Optical Characterization of Transmission Loss, Resonance Tunability, and Gaps. The fabricated waveguides were characterized optically by measuring their transmission spectrum and mode profile. To this end, the samples were inserted into a transmission setup consisting of a horizontally polarized broadband white light source and a spectrometer. In- and outcoupling to the waveguide chip was achieved by two microscope objectives (details in Materials and Methods).

All investigated samples show a core mode formation from the blue to the near-infrared, matching the shape predicted by the numerical simulations (Figure 3c). The recorded spectra show bands with high transmission delimited by resonance dips, reaching contrasts of more than 60 dB for the sample with a 5 cm length. Repeatability of the fabrication is high, as indicated by the light-colored lines in Figures 3 and 4 that represent transmission spectra of copies of the waveguide located on the same chip.

Based on the idea of the cut-back method, we determined the propagation loss of samples with a core size of $D = 20~\mu m$ and SOF of 1% ($L = 176~\mu m$, $G = 2~\mu m$) by measuring the transmission spectrum of samples with different length ranging from 0.5 to 5 cm (Figure 3a). The obtained modal attenuation within the transmission bands in the visible is 0.38−0.72 dB/mm, increasing to 1.25 dB/mm in the IR (1400 nm) for this specific core size and gap length.

According to eq 1, the resonance wavelengths can be tuned by varying the thickness of the polymer walls W. This relationship was experimentally verified by changing the thicknesses of the vertical walls between 600 nm and 2 μm, with step sizes down to 60 nm (circles in Figure 3b). Using eq 1, we calculated the experimentally realized wall thicknesses and verified that the designed step sizes (i.e., thickness increments) were successfully implemented as 62 and 67 nm (samples with wall thicknesses of 1670, 1737, and 1799 nm). The thickness of the horizontal walls was kept fixed to 1.7 μm because a separate experiment showed that resonances corresponding to the horizontal walls are not observable. Evaluating the change of the resonance wavelengths with wall thickness yields tuning slopes between 1.13 nm/nm for the $m = 2$ resonance and 0.25 nm/nm for the $m = 9$ resonance. Remarkable is the large free spectral range of 220 nm in the visible of the sample with 600 nm wall thickness, as shown in the left panel of Figure 3b. This thickness is close to the transverse size of the printed voxel which sets a fundamental size limit to the features realizable by 3D nanoprinting. By calculating the difference between the measured wall thickness and the designed wall thickness, we determined the lateral voxel size to be (358 ± 23) nm for the used printing parameters (see details in Section 2 of the Supporting Information). Note that this estimate does not describe the size of isolated voxels, since the close proximity to other voxels inside the wall influences their size.

Furthermore, we revealed the impact of the gaps on the transmission characteristics by comparing samples with a fixed
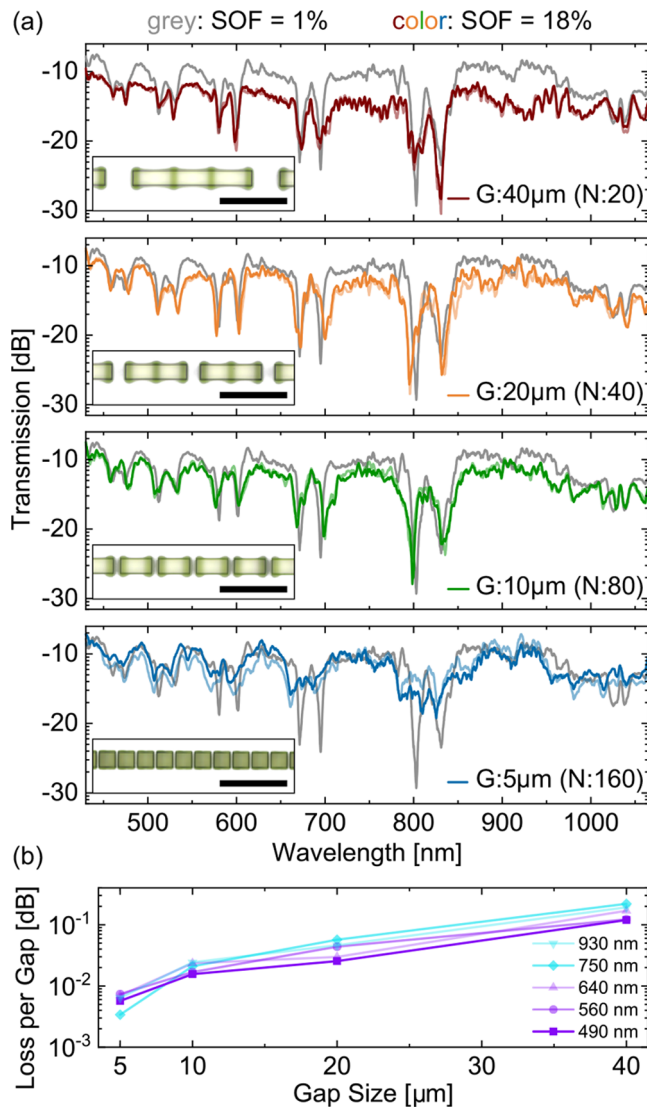

Figure 4. Gap dependence of waveguide transmission. (a) Curves in color show the transmission spectra of samples with different sizes G (5 μm−40 μm) and numbers N (160−20) of gaps such that the total length covered by gaps ($N\cdot G$) is constant, thus fixing the structural openness factor (SOF) to 18%. The gray curve always corresponds to a reference sample with SOF = 1% and otherwise identical properties ($D = 20~\mu m$, $W = 1.75~\mu m$). Values of replicas of a certain structure are shown as curves with lower degree of color saturation. Insets: Transmission microscopy images showing the different gap distributions (scale bar 100 μm). (b) Loss per gap averaged over the wavelength regions of the five transmission bands shown in (a). Each band is labeled by its center wavelength.

SOF of 18% but different distributions of gaps to a reference sample which is nearly completely closed (SOF = 1%, $G = 2$ μm; Figure 4). An overall lower transmission is observed for the samples with larger SOF. For a fixed SOF, the losses decrease when a large number of small gaps is used instead of a few long gaps. The transmission is highest for the shortest gap size of $G = 5~\mu m$ while the resonances are sharpest in the samples with gap sizes of $G = 10−20~\mu m$. The less pronounced resonances for the sample with $G = 5~\mu m$ could be attributed to its short segment length of $L = 23~\mu m$, which might not be enough for the resonances to built up. Assuming that the gap loss of the reference sample with SOF = 1% is negligible, we calculated the loss per gap for each of the investigated
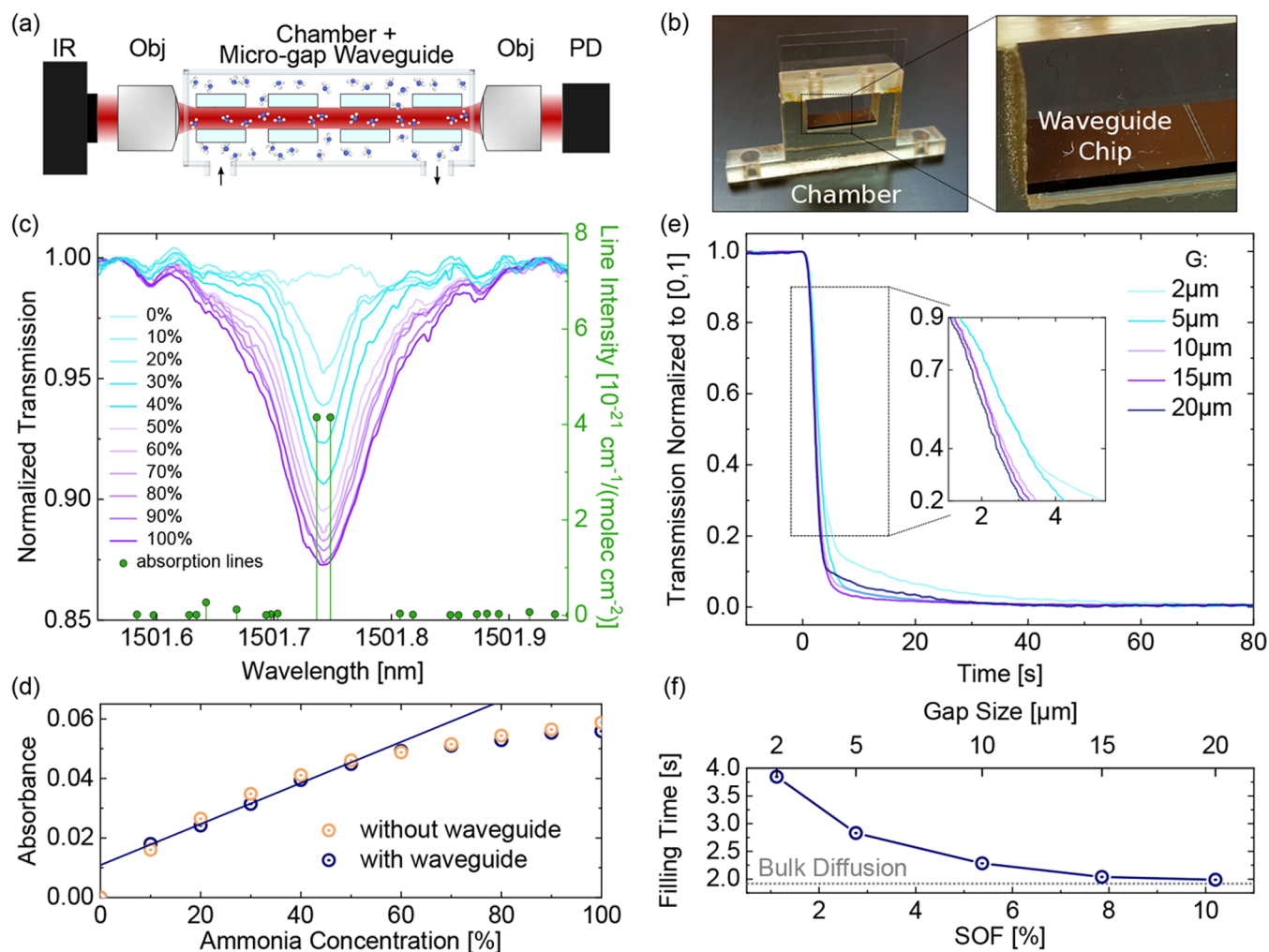
Figure 5. IR gas absorption spectroscopy with microgap waveguide. (a) Schematic of experimental setup illustrating the diffusion of molecules into the waveguide core (IR: tunable infrared laser, Obj: 20× microscope objective, PD: photodetector, arrows: gas in- and outlets). (b) Photographic images of the experimental gas chamber. (c) Waveguide transmission spectra for varying concentrations of ammonia mixed with nitrogen, recorded around a strong ammonia absorption line (λ_0 = 1501.74 nm, green dots: absorption data according to HITRAN database[46,47]). Transmission values larger than one are caused by laser power fluctuations. (d) Corresponding absorbance at λ_0 (blue: measurement from (c), orange: reference measurement without waveguide, blue line: calibration curve). (e) Time-resolved decay of the transmission for different gap sizes G when filling the chamber with 100% ammonia (at λ_0). (f) Filling time of the waveguides shown in (e) as a function of SOF (dotted gray line: filling time of the chamber measured without waveguide).

transmission bands (Figure 4b). The gap loss is lowest for a gap size of $G = 5\ \mu$m with 0.003 dB per gap increasing to 0.22 dB per gap for $G = 40\ \mu$m.

In all recorded transmission spectra, a double dip structure is visible, which most likely arises due to fabrication-related inhomogeneities in the wall thickness. Numerical simulations reveal that surface roughness in the cross-section of the waveguide can lead to a splitting of the resonances, especially toward shorter wavelengths (Figure S1). Another reason might be a slight difference in the wall width between the left and right side of the square shaped cross-section. By fitting a sample spectrum with a two-width model, we determine this difference to be on the order of 50 nm for a wall thickness of 1.55 μm (Table 1, Figure S6).

Gas Sensing with Micro-Gap Waveguides. To demonstrate the practical applicability of microgap waveguides for on-chip sensing devices, gas sensing of ammonia was performed using laser scanning absorption spectroscopy (details can be found in Materials and Methods). Therefore, a target

wavelength of 1501.74 nm was chosen overlapping with a strong absorption line of ammonia.[46,47] The waveguide used here was manufactured with a wall thickness of $W = 1.67\ \mu$m such that the selected absorption line lies in a high transmission region of the sample (Figure S7). Furthermore, the waveguide has a core size of $D = 20\ \mu$m, gap length $G = 10\ \mu$m, segment length $L = 176\ \mu$m, and total length of 5 mm.

The sample was placed into a self-designed gas chamber and a tunable infrared laser provided a monochromatic input beam (see Figure 5a,b) Two microscope objectives enabled in- and outcoupling to the waveguide and a photodetector measuring the outgoing power. Gas mixtures of nitrogen with varying concentrations of ammonia from 10% to 100% were prepared by means of a computer-controlled gas mixing unit to guarantee precise control over the concentration. The measurement was started 2 min after changing the concentration to ensure that the gas inside the chamber was replaced completely.

The results of the measurements are shown in Figure 5c. At the main absorption line (λ_0 = 1501.74 nm) the transmission decreases with increasing ammonia concentration as expected.[36] In order to show the dependency between concentration and absorption, the absorbance at this wavelength was determined by Lambert−Beer's law:[48]

$$A = \log_{10}\left(\frac{P_0}{P}\right) = \epsilon c l \tag{2}$$

with the absorbance A, the incident power P_0, the transmitted power P, the molecular absorption coefficient ϵ, the molar concentration c, and the absorption path length l. To verify that Lambert−Beer's law can be used in its unmodified form, we calculated the fraction of the power of the modal field present inside the polymer walls and thereby cannot be absorbed by the gas (see details in Section 6 of the Supporting Information). As shown in Figure 2c, this fraction is below 10^{-3} within the transmission bands, meaning that virtually all of the field interacts with the gas.

In Figure 5d, the absorbance is shown as a function of the ammonia concentration. As expected, the absorbance increases linearly with concentration for low concentrations between 10% and 50%, while for higher concentrations a saturation can be observed. This trend is also present in a reference measurement with the same gas chamber without the waveguide. As reported elsewhere,[49,50] this saturation can be attributed to collision broadening of the line shape with increasing ammonia concentration, which results in an increase in the area of the absorption dip but not its amplitude. We used the absorbance data for concentrations between 10% and 50% to obtain a linear calibration curve in accordance with eq 2: $A = 6.89 \times 10^{-4} \times c_r + 0.0109$, where c_r is the volume concentration of ammonia in percent. The values of these coefficients agree with the reference measurement within one standard deviation, as expected (details can be found in the Supporting Information, Section 5).

From the calibration curve in Figure 5d, the limit of detection (LoD), meaning the lowest concentration that can be detected in this setup, can be obtained by[51] $\text{LoD} = 3\sigma/s$. Here, σ is the standard deviation of the residuals and s is the slope. For the specific configuration used here we determined a limit of detection of LoD = 3.1%.

To further assess the gas diffusion capabilities, the gas filling time into the core has been determined through dynamic measurements. Specifically, the transmission through waveguides with different gap sizes (G = 2−20 μm, Figure 5e,f) was continuously monitored at one ammonia absorption line (λ_0 = 1501.74 nm). Each measurement started by switching the incoming gas from 100% nitrogen to 100% ammonia. The initial plateau ($t < 0$, $T = 1$ in Figure 5e) appears due to the time the gas needs to flow from the gas mixing unit into the gas chamber. After the waveguide is reached, the transmission shows a rapid decay, indicating diffusion into the different waveguide segments. Note that no further decrease in transmission was observed at any longer time, indicating no further diffusion. The filling times for different gap sizes, defined by the time difference between 90% and 20% of the originally transmitted power (see Materials and Methods for the choice of these values), are shown in Figure 5f. Here, larger gaps lead to a faster decay of the transmission and reach 2 s for the waveguide with 20 μm gaps. This value almost corresponds to the filling time of the gas chamber itself, which was determined in a separate measurement (1.92 s). Note that for

the smallest gap size (G = 2 μm) twice that time is required (all numerical values can be found in the Supporting Information, Section 5). The shoulder in the transmission data, which is visible after the initial decay, results from mechanical compression and decompression of the waveguide, leading to size modulation of the core section and thus the core mode.

■ DISCUSSION

The two presented analytical models are in high agreement with the numerical simulations, with the leaky slab waveguide approach showing the best overlap, especially at IR wavelengths, all of which confirms that antiresonance guidance is the relevant light guidance effect. Note that eq 1 accurately predicts the spectral positions of the resonances (Figures 3b and S2), providing a straightforward pathway to design samples with desired optical properties.

Numerical investigations showed that fabrication inaccuracies such as a rounding of the corners or surface roughness that is uniform along the waveguide axis (e.g., parallel stripes running along the waveguide axis) does not have a strong impact on the waveguide transmission (Figure S1). This is in line with previous findings that the exact shape of the corners of polygonal hollow-core waveguides is irrelevant for its optical properties.[52] Loss due to the introduction of gaps was investigated experimentally and also found to be low with about 10^{-2} dB per gap for gaps shorter than 10 μm. However, the experimentally observed off-resonance loss is about 1 order of magnitude higher than predicted by theory. This could be explained by surface roughness that is nonuniform along the waveguide axis therefore acting as a grating that leads to scattering losses. Preliminary AFM-measurements of the waveguide walls showed that such a roughness is present in the fabricated samples. Future work will target improving the wall uniformity and quality to reach higher levels of transmission, particularly at IR wavelengths. Note that increasing the core size substantially reduces modal attenuation, as for instance observed in antiresonant fibers where losses scale with $1/R^4$ (R: core radius).[37] This phenomenon is different to waveguides that operate on total internal reflection and in which the modal losses are defined by scattering. A further reduction of the loss of the waveguide could principally be achieved by using materials with higher refractive index during the printing process like ceramics or crystalline materials provided that the strong shrinkage of the typically used hybrid organic−inorganic resists during the heat-induced curing can be substantially reduced.[53−57] On the other hand, materials with lower refractive indices like quartz glass might also be beneficial because the losses from surface roughness could be lower[58,59] and the resonances shift less with a varying wall thickness (see eq 1). However, the optical properties of the waveguides also depend to a great extent on the mechanical stability of the resist and the ability to create optically smooth surfaces, making it hard to judge a priori which type of resist is best suited. Overall, the use of inorganic materials would provide better stability of the microgap waveguides against harsh environmental conditions. As shown for light cages, protection against corrosive chemicals can also be provided by coating the nanoprinted structures with alumina nanofilms via low-temperature atomic layer deposition (ALD).[3,60]

The experiments indicate that the introduction of gaps into the waveguide system does not influence the position of the

transmission bands but the magnitude of the overall transmission. For reaching a certain SOF, it seems beneficial to distribute many small gaps along the waveguide axis instead of a few long gaps. Here, we want to point out that beam diffraction of the waveguide mode in the gaps is low since the Rayleigh length of a comparable Gaussian-shaped mode is on the order of 200 μm, which is much longer than the investigated gap sizes. Imperfect terminations of the segments or a manufacturing induced offset between segments perpendicular to the beam axis could further contribute to the gap loss.

The high degree of reproducibility of the transmission spectra of copies of the same waveguide within one chip shows that the 3D nanoprinting process is a highly precise method for manufacturing waveguides.[45] Despite the fact that the voxel size is approximately half the wavelength of the femtosecond laser, subwavelength control of the wall thickness down to 60 nm is possible using nanoprinting (Figure 3b).

Compared to ARROW waveguides, microgap waveguides achieve similar propagation loss and total sample lengths[17,61] while offering simplified fabrication and transverse access to the core region through the gaps. In addition, square-core waveguides are intentionally independent of the polarization direction of the light, which is an advantage over ARROW waveguides which often have rectangular cross sections.[62−65] One particular advantage of microgap waveguides is their large structural openness factor: Waveguide architectures that contain holes that are introduced in a postprocessing step, often reach SOFs of only 0.001−0.005%,[29−31] while in contrast the microgap waveguide reaches SOFs of up to 18%. Such high openness is especially important for diffusion experiments such as low-vapor pressure quantum optics[3] or nanoparticle tracking analysis.[66] It is important to note that the authors recently showed a substantially enhanced level of integration through interfacing nanoprinted light cages with optical fibers on silicon chips,[36] an approach that can be employed to microgap waveguides as well. Another appealing approach is to nanoprint structures directly on the end face of optical fibers, which has been realized for conventional hollow-core waveguide geometries.[67] Note that the shorter sample length of 1 mm and the lack of side-wise openness of these structures might represent a disadvantage for sensing applications. Compared to our previous realization of 3D-nanoprinted waveguides,[35] the propagation loss of microgap waveguides is improved by more than a factor of 2 toward longer wavelengths (λ > 1300 nm) for a similar mode area, a result that we attribute to less surface roughness.

The agreement of the absorption experiments of waveguide and bulk reference measurements (see Section 5 in the Supporting Information) verify that microgap waveguides are principally suitable for gas sensing. From the application perspective, relevant environmental ammonia concentrations are in the order of parts per billion (ppb).[68] In this regard, we would like to point out that in our system, the measured LoD of 3.1% is mainly limited by the detection system and not by the waveguide itself. As reported, for instance, in refs 69 and 70, more advanced detection methods such as wavelength-modulation spectroscopy, lock-in detectors, monitoring of incident laser power, or chemical methods (e.g., spectrophotometric ammonia detection) can be employed to measure ammonia concentrations in the ppb range. For unspecific detection of gases based on refractive index differences, a nanoprinted fiber-integrated microring resonator device has

been demonstrated, being capable of sensing ethanol concentrations down to 0.5 ppm via physisorption.[71] At the waveguide level, the LoD could be further reduced by increasing the waveguide length, leading to larger fringe contrast. Increasing the waveguide length from 5 mm to the maximally investigated length of 5 cm principally allows measuring ten times lower concentrations. Note that while meter-long hollow-core fibers typically have lower detection limits,[72] associated filling times may exceed practically feasible limits. Here, microgap waveguides can be directly immersed in the analyte, which can transversely enter the core section. The decay of transmission, which is visible in the dynamic measurements (Figure 5e), is basically composed of three contributions: (i) filling time of the gas chamber, (ii) bulk diffusion into the free areas between the segments, and (iii) restricted diffusion into the cores of the segments themselves. Due to the latter, the samples with small SOF show a slower diffusion (delay up to 2 s) compared to the chamber itself. This is in contrast to the samples with the largest SOF (about 10%), filling up nearly as fast as the gas chamber. Therefore, we attribute the decrease in filling time for larger gap sizes G to the fact that these samples allow more bulk-type diffusion (see Table S2 of the Supporting Information for details). A further reduction of the filling time can be achieved by using even larger gaps or local modification of the microgap waveguide (e.g., perforation or partial opening of the segments), which can be easily realized by means of the 3D nanoprinting process.

Compared to the light cage concept, the microgap waveguide presented here has several key advantages, such as simplified and faster fabrication by 3D nanoprinting in Cartesian coordinates, one-step implementation of longer waveguides (up to 5 cm), or much lower losses in the infrared (1.25 vs 3 dB/mm @ 1400 nm). From the optical perspective, improved optical properties result from much wider spectral transmission windows (>200 nm) and much more pronounced resonances (>60 dB). With the same optical losses (approximately 0.5 dB/mm), the microgap waveguide has decisive advantages over ARROWs, such as lateral access and thus significantly faster diffusion and the avoidance of costly and time-consuming multistep manufacturing processes by using 3D nanoprinting.

■ CONCLUSION

In this work, a novel type of integrated on-chip hollow-core waveguide that shows strong light-gas interaction over centimeter distances is introduced. The waveguide design consists of two types of segments alternating on the micrometer scale: (i) square shaped hollow waveguide segments consisting of 20 μm cores enclosed by submicrometer polymer walls and (ii) open gap regions between adjacent elements for externally accessing the core region. Samples with lengths up 5 cm on silicon chips have been implemented through 3D-nanoprinting, avoiding time-consuming multistep fabrication procedures. As confirmed by mathematical models and full numerical simulations, light guidance in this type of waveguide is based on the antiresonance effect, which is reflected in a characteristic transmission distribution. Our study includes full optical characterization, revealing modal loss, impact of gap size, and spectral tuning potential. Examples of highlights include operation from visible to near-infrared wavelengths, extremely broadband transmission windows (>200 nm), clear resonance dips with exceptionally high fringe contrasts (>60 dB), low loss per gap (0.003 dB), and

Table 1. Overview of the Different Types of Fabrication Inaccuracies

type of inaccuracy	effect	magnitude
surface roughness (constant average wall thickness)	broadening of resonances, increased loss	not studied rigorously in this work, 30−40 nm reported in other works[67,76]
wall thickness differences within structure (e.g., different thickness of left and right wall)	splitting of resonances	50 nm[this work]
batch-to-batch (chip-to-chip) variations (different average thickness of the wall for different batches)	shifting of resonances	15 nm reported for light cages[45]

controlling resonance wavelengths through precise nano-printing with successfully implemented step sizes (i.e., increments) in wall thickness of 60 nm. Particularly note-worthy is the exceptionally large structural opening factor of 18%, exceeding those of perforated waveguides by more than thousand. The application potential was demonstrated in the context of laser-scanning absorption spectroscopy of ammonia, showing fast diffusion speeds nearly indistinguishable to bulk type diffusion in cuvettes and a limit of detection that lies in the order of other reported devices. Due to these unique properties, application of the on-chip antiresonant hollow-core microgap waveguide can be expected in a variety of fields related to integrated spectroscopy, including bioanalytics (e.g., detection of contamination), environmental sciences (e.g., gas analysis) and life sciences (e.g., nanoparticle tracking analysis). Note that operation in liquids, particularly in water, is straightforward to achieve due to the flexibility of the light guidance effect and has been demonstrated on the example of optofluidic light cage[73] Here, 3D nanoprinting offers unique opportunities in terms of implementing customized on-chip hollow-core waveguides, examples of which include the introduction of local modification already in the fabrication step, or the implementation of geometries with cross sections that vary along the waveguide axis, all of which making the presented waveguide a promising alternative to ARROWs.

■ MATERIALS AND METHODS

Fabrication. The microgap waveguides were realized on polished silicon substrates by two-photon-polymerization of liquid IP-Dip photoresist using a commercial 3D nanoprinting system (Photonic Professional GT, Nanoscribe GmbH). Compared to other 3D additive manufacturing techniques such as direct ink writing or electrohydrodynamic redox printing, only two-photon-polymerization can reach the required small voxel size while retaining printing speeds sufficient for creating centimeter-long waveguides.[74] To this end, the dip-in configuration of the system was used where a high numerical aperture objective (Plan-Apochromat 63×/1.40 Oil DIC, Zeiss) is immersed directly into the resist. Femtosecond laser pulses with a center wavelength of 780 nm, repetition rate of 80 MHz and pulse length of 100 fs are focused through the objective to induce polymerization of the resist. Individual waveguide segments are built up layer-by-layer, laterally, by scanning the focused laser beam using a galvanometric mirror and axially by piezo-driven displacement of the substrate. Due to the occurrence of aberrations and a decrease in intensity toward the edges of the print field, the maximum length of individual segments was limited to 180 μm. Subsequently, the substrate is shifted along the waveguide axis by means of a mechanical stage, either leaving a gap to the previous segment or linking two segments with an overlap of 10 μm to realize segments lengths larger than 180 μm. Artifacts arising from the stitching process were minimized by calibrating the mechanical stage and could further be improved by using stitch-free nanoprinting where mechanical stage and galvanometric mirror move in sync.[75] Typical printing parameters were 37 mW, 70000 μm/s, 1 V/ms^2, and 150 nm/200 nm for laser power, scanning speed, mirror acceleration, and hatching/slicing distances, respectively. Please note that the reported value for the acceleration of the galvanometric mirror is only applicable within the framework of machines by Nanoscribe GmbH. Generally, a low mirror acceleration should be used to achieve a high quality of the edges of the printed structures. The maximum spacing between blocks in order for the structure to be stable was determined to be 60 μm. After laser-exposure, the unpolymerized resist was removed by immersion in propylene glycol monomethyl ether acetate (PGMEA, Sigma-Aldrich) for 30 min and methoxy-nonafluorobutane (Novec 7100 Engineered Fluid, 3M) for 15 min, followed by evaporative drying in air.

Optical Characterization Setup. The optical characterization of the samples was carried out on two setups. The setups consist of a broadband white light source (SuperK Fianium, NKT Photonics; SuperK Compact, NKT Photonics), in- and outcoupling objectives mounted on 3D translation stages (Nikon, 10×, NA = 0.3; Olympus, 20×, NA = 0.4; Olympus, 10×, NA = 0.25), a CCD for imaging the waveguide mode and a spectrometer (Princeton Instruments, grating period: 300 g/mm, blaze angle: 750 nm, spectral resolution: $\Delta\lambda$ = 0.13 nm; Ando optical spectrum analyzer AQ-6315A) connected to a multimode-fiber (M15L05, core size: 105 μm, NA: 0.22; M42L05, core size: 50 μm, NA: 0.22). Both setups employ a polarizer to obtain a horizontally polarized beam from the white light source. One setup uses a system to improve the beam quality, including a beam expansion stage combined with a pinhole. The other system includes a notch filter to block the pump laser of the supercontinuum source at 1060 nm. The coupling to the fundamental mode of the waveguide is optimized by beam steering and shifting the objective on the 3D translation stage. The process is monitored by imaging the core mode onto a CCD optimizing for highest CCD pixel intensity while preserving the shape of the fundamental mode. In a second step, the power coupled to the fiber of the spectrometer is maximized.

All recorded spectra are normalized to a reference spectrum taken without a sample and the objectives moved closer together to compensate for the missing length of the waveguide. Mode images at different wavelengths were recorded using the wavelength selector of the supercontinuum source, which features a bandwidth of approximately 10 nm.

Gas Absorption Measurement. The setup for the ammonia gas sensing consists of a tunable diode laser (TUNICS 1550, Photonetics), two microscope objectives for in- and outcoupling (Edmund, 20×, NA = 0.4; Olympus, 10×, NA = 0.25), a CCD (ABS, IK1513), and a photodiode (Thorlabs, S122C) to monitor the outgoing power. Both objectives are mounted on 3D translation stages to enable the

coupling to the fundamental mode of the waveguide. The CCD is used to check if the coupling is successful. In this case, a clear core mode with hexagonal symmetry can be observed. In a computer-controlled gas mixer (Qcal, GMS_4CH_HP) different compositions of ammonia and nitrogen were prepared with the gas flow set to 75 sccm. From there the gas mixture flows through a tube to the inlet of a self-designed 3D-printed gas chamber while the outlet is open to ambient air. The windows of the gas chamber are made of borosilicate glass and have a thickness of around 0.15 mm. For the spectroscopic measurement, the laser wavelength was swept through the wavelength region of 1501.55 to 1501.95 nm with a step size of 1 pm. The bandwidth of that laser is 100 kHz which is well below the used step size. Each spectrum was normalized to an individual linear baseline, that connects the transmission values at the border of the region of interest (1501.57 and 1501.93 nm). Each measurement took around 3 min. Note that this duration is limited by the scanning speed of the tunable laser. For the dynamic measurement, the transmission wavelength remained constant at the main absorption line of ammonia (λ_0 = 1501.74 nm). The filling times were then determined as the time difference between reaching 90% and 20% of the original transmitted power. Those limits were chosen to suppress the effect of fluctuations at the beginning of the measurement and the shoulder after the initial decay. For a better overview, all data from the dynamic measurements were rescaled, while for all gap sizes, the transmission drop is about 15%, which is in accordance with the static measurements for 100% ammonia concentration (purple curve in Figure 5c). The specifications of the different experiments can be found in the Supporting Information, Section 5.

Numerical Simulation. Numerical simulations were carried out using a commercial finite element solver (COMSOL Multiphysics, RF module). The waveguide was assumed to be continuous along the propagation axis, that is, the effect of gaps is neglected. Using the Cartesian symmetry of the waveguide, the eigenvalues of one quarter of its two-dimensional cross section were calculated using perfect-electrical conductor and perfect magnetic conductor boundary conditions along the vertical and horizontal symmetry lines, respectively. Perfectly matched layers were employed at the remaining two boundaries. The predictions of the analytical model along with manual selection were used to identify the one-lobed fundamental mode. The Sellmeier coefficients for the dispersion of the polymer were taken from Table 2 in a work on the optical properties of photoresists.[77] Material absorption in the investigated wavelength range is low and was not considered. All waveguides were simulated with a core size of D = 20 μm and wall thickness of W = 1 μm. For Figure 2, a rounding radius of 2 μm was used to account for fabrication inaccuracies. For the simulation of the surface roughness in Figure S1, a sinusoidal roughness term was applied to the 2D cross section of the waveguide with a periodicity of 200 nm and an amplitude of 100 nm for the vertical walls and a periodicity of 150 nm and an amplitude of 200 nm for the horizontal walls, accounting for the different slicing/hatching distances and the ellipsoidal voxel shape. In order to compensate for the additional material, the wall thickness of the vertical walls was reduced to 856 nm and to 793 nm for the horizontal walls.

Analytical Models. A complete description of the two analytical models for light guidance in hollow square core

antiresonant waveguides, assuming uniformity along the propagation direction, can be found in Section 3 of the Supporting Information.

■ ASSOCIATED CONTENT

ⓈI Supporting Information

The Supporting Information is available free of charge at https://pubs.acs.org/doi/10.1021/acsphotonics.2c00725.

> In-depth description of the two analytical models, details of the gas sensing experiment, including diffusion simulations, model for double-dip resonance structure, simulations of fabrication inaccuracies, and fraction of power located inside the polymer, and evaluation of the voxel size (PDF)

■ AUTHOR INFORMATION

Corresponding Author

　Johannes Bürger − *Chair in Hybrid Nanosystems, Nanoinstitute Munich, Ludwig-Maximilians-Universität Munich, 80539 Munich, Germany;* ⓞ orcid.org/0000-0003-4821-1790; Email: j.buerger@physik.uni-muenchen.de

Authors

　Vera Schalles − *Leibniz Institute of Photonic Technology, 07745 Jena, Germany; Abbe Center of Photonics and Faculty of Physics, Friedrich-Schiller-Universität Jena, 07743 Jena, Germany*

　Jisoo Kim − *Leibniz Institute of Photonic Technology, 07745 Jena, Germany; Abbe Center of Photonics and Faculty of Physics, Friedrich-Schiller-Universität Jena, 07743 Jena, Germany;* ⓞ orcid.org/0000-0001-6785-0446

　Bumjoon Jang − *Leibniz Institute of Photonic Technology, 07745 Jena, Germany; Abbe Center of Photonics and Faculty of Physics, Friedrich-Schiller-Universität Jena, 07743 Jena, Germany*

　Matthias Zeisberger − *Leibniz Institute of Photonic Technology, 07745 Jena, Germany; Abbe Center of Photonics and Faculty of Physics, Friedrich-Schiller-Universität Jena, 07743 Jena, Germany*

　Julian Gargiulo − *Chair in Hybrid Nanosystems, Nanoinstitute Munich, Ludwig-Maximilians-Universität Munich, 80539 Munich, Germany;* ⓞ orcid.org/0000-0002-4524-3423

　Leonardo de S. Menezes − *Chair in Hybrid Nanosystems, Nanoinstitute Munich, Ludwig-Maximilians-Universität Munich, 80539 Munich, Germany; Departmento de Física, Universidade Federal de Pernambuco, 50670-901 Recife, PE, Brazil;* ⓞ orcid.org/0000-0002-8654-1953

　Markus A. Schmidt − *Leibniz Institute of Photonic Technology, 07745 Jena, Germany; Otto Schott Institute of Materials Research (OSIM), Friedrich-Schiller-Universität Jena, 07743 Jena, Germany; Abbe Center of Photonics and Faculty of Physics, Friedrich-Schiller-Universität Jena, 07743 Jena, Germany;* ⓞ orcid.org/0000-0002-5324-6405

　Stefan A. Maier − *School of Physics and Astronomy, Monash University, Clayton, Victoria 3800, Australia; Chair in Hybrid Nanosystems, Nanoinstitute Munich, Ludwig-Maximilians-Universität Munich, 80539 Munich, Germany; The Blackett Laboratory, Department of Physics, Imperial College London, London SW7 2AZ,, United Kingdom;* ⓞ orcid.org/0000-0001-9704-7902

Complete contact information is available at:

■ REFERENCES

(1) Kumar, P.; Morawska, L.; Martani, C.; Biskos, G.; Neophytou, M.; Di Sabatino, S.; Bell, M.; Norford, L.; Britter, R. The rise of low-cost sensing for managing air pollution in cities. *Environ. Int.* **2015**, *75*, 199−205.

(2) Lawal, O.; Ahmed, W. M.; Nijsen, T. M. E.; Goodacre, R.; Fowler, S. J. Exhaled breath analysis: a review of 'breath-taking' methods for off-line analysis. *Metabolomics* **2017**, *13*, 110.

(3) Davidson-Marquis, F.; Gargiulo, J.; Gómez-López, E.; Jang, B.; Kroh, T.; Müller, C.; Ziegler, M.; Maier, S.; Kübler, H.; Schmidt, M.; Benson, O. Coherent interaction of atoms with a beam of light confined in a light cage. *Light: Sci. Appl.* **2021**, *10*, 114.

(4) Epping, J. P.; Hellwig, T.; Hoekman, M.; Mateman, R.; Leinse, A.; Heideman, R. G.; van Rees, A.; van der Slot, P. J.; Lee, C. J.; Fallnich, C.; Boller, K.-J. On-chip visible-to-infrared supercontinuum generation with more than 495 THz spectral bandwidth. *Opt. Express* **2015**, *23*, 19596−19604.

(5) Kuyken, B.; Ideguchi, T.; Holzner, S.; Yan, M.; Haensch, T.; Van Campenhout, J.; Verheyen, P.; Coen, S.; Leo, F.; Baets, R.; Roelkens, G.; Picqué, N. An octave spanning mid-infrared frequency comb generated in a silicon nanophotonic wire waveguide. *Nat. Commun.* **2015**, *6*, 6310.

(6) Roelkens, G.; Liu, L.; Liang, D.; Jones, R.; Fang, A.; Koch, B.; Bowers, J. III-V/silicon photonics for on-chip and intra-chip optical interconnects. *Laser Photonics Rev.* **2010**, *4*, 751−779.

(7) Pohl, D.; Reig Escalé, M.; Madi, M.; Kaufmann, F.; Brotzer, P.; Sergeyev, A.; Guldimann, B.; Giaccari, P.; Alberti, E.; Meier, U.; Grange, R. An integrated broadband spectrometer on thin-film lithium niobate. *Nat. Photonics* **2020**, *14*, 24−29.

(8) Kita, D.; Miranda, B.; Favela, D.; Bono, D.; Michon, J.; Lin, H.; Gu, T.; Hu, J. High-performance and scalable on-chip digital Fourier transform spectroscopy. *Nat. Commun.* **2018**, *9*, 4405.

(9) Souza, M.; Grieco, A.; Frateschi, N.; Fainman, Y. Fourier transform spectrometer on silicon with thermo-optic non-linearity and dispersion correction. *Nat. Commun.* **2018**, *9*, 665.

(10) Gao, H.; Chen, G. F. R.; Xing, P.; Choi, J. W.; Low, H. Y.; Tan, D. T. H. High-Resolution 3D Printed Photonic Waveguide Devices. *Adv. Opt. Mater.* **2020**, *8*, 2000613.

(11) Doherty, B.; Csáki, A.; Thiele, M.; Zeisberger, M.; Schwuchow, A.; Kobelke, J.; Fritzsche, W.; Schmidt, M. A. Nanoparticle functionalised small-core suspended-core fibre - a novel platform for efficient sensing. *Biomed. Opt. Express* **2017**, *8*, 790−799.

(12) Doherty, B.; Thiele, M.; Warren-Smith, S.; Schartner, E.; Ebendorff-Heidepriem, H.; Fritzsche, W.; Schmidt, M. A. Plasmonic nanoparticle-functionalized exposed-core fiber- an optofluidic refractive index sensing platform. *Opt. Lett.* **2017**, *42*, 4395−4398.

(13) Chemnitz, M.; Schmidl, G.; Schwuchow, A.; Zeisberger, M.; Hübner, U.; Weber, K.; Schmidt, M. A. Enhanced sensitivity in single-mode silicon nitride stadium resonators at visible wavelengths. *Opt. Lett.* **2016**, *41*, 5377−5380.

(14) Tombez, L.; Zhang, E. J.; Orcutt, J. S.; Kamlapurkar, S.; Green, W. M. J. Methane absorption spectroscopy on a silicon photonic chip. *Optica* **2017**, *4*, 1322−1325.

(15) Stern, L.; Desiatov, B.; Mazurski, N.; Levy, U. Strong coupling and high contrast all optical modulation in atomic cladding waveguides. *Nat. Commun.* **2017**, *8*, 14461.

(16) Duguay, M. A.; Kokubun, Y.; Koch, T. L.; Pfeiffer, L. Antiresonant reflecting optical waveguides in SiO2-Si multilayer structures. *Appl. Phys. Lett.* **1986**, *49*, 13−15.

(17) Yin, D.; Schmidt, H.; Barber, J.; Hawkins, A. Integrated ARROW waveguides with hollow cores. *Opt. Express* **2004**, *12*, 2710−2715.

(18) Yin, D.; Barber, J. P.; Hawkins, A. R.; Schmidt, H. Waveguide loss optimization in hollow-core ARROW waveguides. *Opt. Express* **2005**, *13*, 9331−9336.

(19) Hartung, A.; Kobelke, J.; Schwuchow, A.; Bierlich, J.; Popp, J.; Schmidt, M. A.; Frosch, T. Low-loss single-mode guidance in large-core antiresonant hollow-core fibers. *Opt. Lett.* **2015**, *40*, 3432−3435.

(20) Belardi, W. Hollow-Core Optical Fibers. *Fibers* **2019**, *7*, 50.

(21) Belardi, W. Design and Properties of Hollow Antiresonant Fibers for the Visible and Near Infrared Spectral Range. *J. Lightwave Technol.* **2015**, *33*, 4497−4503.

(22) Masum, B. M.; Aminossadati, S. M.; Kizil, M. S.; Leonardi, C. R. Numerical and experimental investigations of pressure-driven gas flow in hollow-core photonic crystal fibers. *Appl. Opt.* **2019**, *58*, 963−972.

(23) Sprague, M.; Michelberger, P.; Champion, T.; England, D.; Nunn, J.; Jin, X.-M.; Kolthammer, W.; Abdolvand, A.; Russell, P.; Walmsley, I. Broadband single-photon-level memory in a hollow-core photonic crystal fibre. *Nat. Photonics* **2014**, *8*, 287−291.

(24) Kaczmarek, K. T.; Saunders, D. J.; Sprague, M. R.; Kolthammer, W. S.; Feizpour, A.; Ledingham, P. M.; Brecht, B.; Poem, E.; Walmsley, I. A.; Nunn, J. Ultrahigh and persistent optical depths of cesium in Kagomé-type hollow-core photonic crystal fibers. *Opt. Lett.* **2015**, *40*, 5582−5585.

(25) Säynätjoki, A.; Karvonen, L.; Alasaarela, T.; Tu, X.; Liow, T.-Y.; Hiltunen, M.; Tervonen, A.; Lo, G. Q.; Honkanen, S. K. Low-loss silicon slot waveguides and couplers fabricated with optical lithography and atomic layer deposition. *Opt. Express* **2011**, *19*, 26275−82.

(26) Barrios, C. A.; Gylfason, K. B.; Sánchez, B.; Griol, A.; Sohlström, H.; Holgado, M.; Casquel, R. Slot-waveguide biochemical sensor. *Opt. Lett.* **2007**, *32*, 3080−3082.

(27) Sun, H.; Chen, A.; Dalton, L. Enhanced Evanescent Confinement in Multiple-Slot Waveguides and its Application in Biochemical Sensing. *IEEE Photonics J.* **2009**, *1*, 48−57.

(28) Gnewuch, H.; Renner, H. Mode-independent attenuation in evanescent-field sensors. *Appl. Opt.* **1995**, *34*, 1473−1483.

(29) Hoo, Y. L.; Liu, S.; Ho, H. L.; Jin, W. Fast Response Microstructured Optical Fiber Methane Sensor With Multiple Side-Openings. *IEEE Photonics Technol. Lett.* **2010**, *22*, 296−298.

(30) Hensley, C. J.; Broaddus, D. H.; Schaffer, C. B.; Gaeta, A. L. Photonic band-gap fiber gas cell fabricated using femtosecond micromachining. *Opt. Express* **2007**, *15*, 6690−6695.

(31) Yang, F.; Jin, W.; Lin, Y.; Wang, C.; Lut, H.; Tan, Y. Hollow-Core Microstructured Optical Fiber Gas Sensors. *J. Lightwave Technol.* **2017**, *35*, 3413−3424.

(32) Cordeiro, C. M. B.; dos Santos, E. M.; Cruz, C. H. B.; de Matos, C. J. S.; Ferreira, D. S. Lateral access to the holes of photonic crystal fibers − selective filling and sensing applications. *Opt. Express* **2006**, *14*, 8403−8412.

(33) Giraud-Carrier, M.; Hill, C.; Decker, T.; Black, J. A.; Schmidt, H.; Hawkins, A. Perforated hollow-core optical waveguides for on-chip atomic spectroscopy and gas sensing. *Appl. Phys. Lett.* **2016**, *108*, 131105.

(34) Holmes, M. R. Micropore and nanopore fabrication in hollow antiresonant reflecting optical waveguides. *J. Micro/Nanolithogr., MEMS, MOEMS* **2010**, *9*, 023004.

(35) Jain, C.; Braun, A.; Gargiulo, J.; Jang, B.; Li, G.; Lehmann, H.; Maier, S. A.; Schmidt, M. A. Hollow Core Light Cage: Trapping Light Behind Bars. *ACS Photonics* **2019**, *6*, 649−658.

(36) Jang, B.; Gargiulo, J.; Kim, J.; Bürger, J.; Both, S.; Lehmann, H.; Wieduwilt, T.; Weiss, T.; Maier, S. A.; Schmidt, M. A. Fiber-integrated hollow-core light cage for gas spectroscopy. *APL Photonics* **2021**, *6*, 061301.

(37) Zeisberger, M.; Schmidt, M. Analytic model for the complex effective index of the leaky modes of tube-type anti-resonant hollow core fibers. *Sci. Rep.* **2017**, *7*, 11761.

(38) Litchinitser, N. M.; Abeeluck, A. K.; Headley, C.; Eggleton, B. J. Antiresonant reflecting photonic crystal optical waveguides. *Opt. Lett.* **2002**, *27*, 1592−1594.

(39) Hartung, A.; Kobelke, J.; Schwuchow, A.; Wondraczek, K.; Bierlich, J.; Popp, J.; Frosch, T.; Schmidt, M. A. Double antiresonant hollow core fiber − guidance in the deep ultraviolet by modified tunneling leaky modes. *Opt. Express* **2014**, *22*, 19131−19140.

(40) Russell, P. Photonic Crystal Fibers. *Science* **2003**, *299*, 358−362.

(41) Sollapur, R.; Kartashov, D.; Zuerch, M.; Hoffmann, A.; Grigorova, T.; Sauer, G.; Hartung, A.; Schwuchow, A.; Bierlich, J.; Kobelke, J.; Chemnitz, M.; Schmidt, M.; Spielmann, C. Resonance-enhanced multi-octave supercontinuum generation in antiresonant hollow-core fibers. *Light: Sci. Appl.* **2017**, *6*, No. e17124.

(42) Pryamikov, A. D.; Biriukov, A. S.; Kosolapov, A. F.; Plotnichenko, V. G.; Semjonov, S. L.; Dianov, E. M. Demonstration of a waveguide regime for a silica hollow - core microstructured optical fiber with a negative curvature of the core boundary in the spectral region > *rbin*3.5 *μ*m. *Opt. Express* **2011**, *19*, 1441−1448.

(43) Okamoto, K. *Fundamentals of Optical Waveguides*; Academic Press, 2006.

(44) Ando, R. F.; Hartung, A.; Jang, B.; Schmidt, M. A. Approximate model for analyzing band structures of single-ring hollow-core anti-resonant fibers. *Opt. Express* **2019**, *27*, 10009−10021.

(45) Bürger, J.; Kim, J.; Jang, B.; Gargiulo, J.; Schmidt, M. A.; Maier, S. A. Ultrahigh-aspect-ratio light cages: fabrication limits and tolerances of free-standing 3D nanoprinted waveguides. *Opt. Mater. Express* **2021**, *11*, 1046−1057.

(46) HITRAN Database. https://hitran.org/ (accessed 2022−07−20).

(47) Sung, K.; Brown, L.; Huang, X.; Schwenke, D.; Lee, T.; Coy, S.; Lehmann, K. Extended line positions, intensities, empirical lower state energies and quantum assignments of NH3 from 6300 to 7000 cm^{-1}. *J. Quant. Spectrosc. Radiat. Transfer* **2012**, *113*, 1066−1083.

(48) Braslavsky, S. E. Glossary of terms used in photochemistry, 3rd edition (IUPAC Recommendations 2006). *Pure Appl. Chem.* **2007**, *79*, 293−465.

(49) Webber, M. E. *Diode Laser Measurements of Ammonia and Carbon Dioxide for Combustion and Bioreactor Applications*; Stanford University, 2001.

(50) Webber, M. E.; Baer, D. S.; Hanson, R. K. Ammonia monitoring near 1.5 *μ*m with diode-laser absorption sensors. *Appl. Opt.* **2001**, *40*, 2031−2042.

(51) Şengül, Ü. Comparing determination methods of detection and quantification limits for aflatoxin analysis in hazelnut. *J. Food Drug Anal.* **2016**, *24*, 56−62.

(52) Pryamikov, A. D.; Alagashev, G. K.; Kosolapov, A. F.; Biriukov, A. S. Impact of core-cladding boundary shape on the waveguide properties of hollow core microstructured fibers. *Laser Phys.* **2016**, *26*, 125104.

(53) Merkininkaitė, G.; Aleksandravičius, E.; Malinauskas, M.; Gailevičius, D.; Šakirzanovas, S. Laser additive manufacturing of Si/ZrO$_2$ tunable crystalline phase 3D nanostructures. *Opto-Electron. Adv.* **2022**, *5*, 210077.

(54) Gonzalez-Hernandez, D.; Varapnickas, S.; Merkininkaitė, G.; Čiburys, A.; Gailevičius, D.; Šakirzanovas, S.; Juodkazis, S.; Malinauskas, M. Laser 3D Printing of Inorganic Free-Form Micro-Optics. *Photonics* **2021**, *8*, 577.

(55) Konstantinou, G.; Kakkava, E.; Hagelüken, L.; Warriam Sasikumar, P. V.; Wang, J.; Makowska, M. G.; Blugan, G.; Nianias, N.; Marone, F.; Van Swygenhoven, H.; Brugger, J.; Psaltis, D.; Moser, C. Additive micro-manufacturing of crack-free PDCs by two-photon polymerization of a single, low-shrinkage preceramic resin. *Addit. Manuf.* **2020**, *35*, 101343.

(56) Brigo, L.; Schmidt, J. E. M.; Gandin, A.; Michieli, N.; Colombo, P.; Brusatin, G. 3D Nanofabrication of SiOC Ceramic Structures. *Adv. Sci. (Weinheim, Ger.)* **2018**, *5*, 1800937.

(57) Vyatskikh, A.; Ng, R. C.; Edwards, B.; Briggs, R. M.; Greer, J. R. Additive Manufacturing of High-Refractive-Index, Nanoarchitected Titanium Dioxide for 3D Dielectric Photonic Crystals. *Nano Lett.* **2020**, *20*, 3513−3520.

(58) Johnson, S.; Povinelli, M.; Soljačić, M.; Karalis, A.; Jacobs, S.; Joannopoulos, J. Roughness losses and volume-current methods in photonic-crystal waveguides. *Appl. Phys. B: Lasers Opt.* **2005**, *81*, 283−293.

(59) Fokoua, E. N.; Poletti, F.; Richardson, D. J. Analysis of light scattering from surface roughness in hollow-core photonic bandgap fibers. *Opt. Express* **2012**, *20*, 20980−20991.

(60) Jang, B.; Gargiulo, J.; Ziegler, M.; Ando, R. F.; Hübner, U.; Maier, S. A.; Schmidt, M. A. Fine-tuning of the optical properties of hollow-core light cages using dielectric nanofilms. *Opt. Lett.* **2020**, *45*, 196−199.

(61) Yin, D.; Schmidt, H.; Barber, J. P.; Lunt, E. J.; Hawkins, A. R. Optical characterization of arch-shaped ARROW waveguides with liquid cores. *Opt. Express* **2005**, *13*, 10564−10570.

(62) Bernini, R.; Nuccio, E.; Minardo, A.; Zeni, L.; Sarro, P. Integrated silicon optical sensors based on hollow core waveguide. *Proc. SPIE* **2007**, *6477*, 647714.

(63) Bernini, R.; Campopiano, S.; Zeni, L.; Sarro, P. M. ARROW optical waveguides based sensors. *Sens. Actuators, B* **2004**, *100*, 143−146.

(64) Yang, W.; Conkey, D.; Wu, B.; Yin, D.; Hawkins, A.; Schmidt, H. Atomic spectroscopy on a chip. *Nat. Photonics* **2007**, *1*, 331−335.

(65) Schmidt, H.; Hawkins, A. R. Optofluidic waveguides: I. Concepts and implementations. *Microfluid. Nanofluid.* **2008**, *4*, 3−16.

(66) Förster, R.; Weidlich, S.; Nissen, M.; Wieduwilt, T.; Kobelke, J.; Goldfain, A. M.; Chiang, T. K.; Garmann, R. F.; Manoharan, V. N.; Lahini, Y.; Schmidt, M. A. Tracking and Analyzing the Brownian Motion of Nano-objects Inside Hollow Core Fibers. *ACS Sens* **2020**, *5*, 879−886.

(67) Bertoncini, A.; Liberale, C. 3D printed waveguides based on photonic crystal fiber designs for complex fiber-end photonic devices. *Optica* **2020**, *7*, 1487−1494.

(68) Dragosits, U.; Theobald, M.; Place, C.; Lord, E.; Webb, J.; Hill, J.; ApSimon, H.; Sutton, M. Ammonia emission, deposition and impact assessment at the field scale: a case study of sub-grid spatial variability. *Environ. Pollut.* **2002**, *117*, 147−158.

(69) Wang, J.; Zhang, W.; Li, L.; Yu, Q. Breath ammonia detection based on tunable fiber laser photoacoustic spectroscopy. *Appl. Phys. B: Laser Opt.* **2011**, *103*, 263−269.

(70) Timmer, B.; Olthuis, W.; van den Berg, A. Ammonia sensors and their applications—a review. *Sens. Actuators, B* **2005**, *107*, 666−677.

(71) Melissinaki, V.; Tsilipakos, O.; Kafesaki, M.; Farsari, M.; Pissadakis, S. Micro-Ring Resonator Devices Prototyped on Optical Fiber Tapers by Multi-Photon Lithography. *IEEE J. Sel. Top. Quantum Electron.* **2021**, *27*, 1−7.

(72) Nikodem, M.; Gomółka, G.; Klimczak, M.; Pysz, D.; Buczyński, R. Demonstration of mid-infrared gas sensing using an anti-resonant hollow core fiber and a quantum cascade laser. *Opt. Express* **2019**, *27*, 36350−36357.

(73) Kim, J.; Jang, B.; Gargiulo, J.; Bürger, J.; Zhao, J.; Upendar, S.; Weiss, T.; Maier, S. A.; Schmidt, M. A. The Optofluidic Light Cage − On-Chip Integrated Spectroscopy Using an Antiresonance Hollow Core Waveguide. *Anal. Chem.* **2021**, *93*, 752−760.

(74) Hahn, V.; Kiefer, P.; Frenzel, T.; Qu, J.; Blasco, E.; Barner-Kowollik, C.; Wegener, M. Rapid Assembly of Small Materials Building Blocks (Voxels) into Large Functional 3D Metamaterials. *Adv. Funct. Mater.* **2020**, *30*, 1907795.

(75) Jonušauskas, L.; Gailevičius, D.; Rekštytė, S.; Baldacchini, T.; Juodkazis, S.; Malinauskas, M. Mesoscale laser 3D printing. *Opt. Express* **2019**, *27*, 15205−15221.

(76) Dietrich, P.-I.; Blaicher, M.; Reuter, I.; Billah, M.; Hoose, T.; Hofmann, A.; Caer, C.; Dangel, R.; Offrein, B.; Troppenz, U.; Moehrle, M.; Freude, W.; Koos, C. In-Situ 3D Nano-Printing of Freeform Coupling Elements for Hybrid Photonic Integration. *Nat. Photonics* **2018**, *12*, 241−247.

(77) Schmid, M.; Ludescher, D.; Giessen, H. Optical properties of photoresists for femtosecond 3D printing: refractive index, extinction, luminescence-dose dependence, aging, heat treatment and comparison between 1-photon and 2-photon exposure. *Opt. Mater. Express* **2019**, *9*, 4564−4577.

▣ Recommended by ACS